Liquid and Crystal Phases of Dipolar Fermions in Two Dimensions

N. Matveeva and S. Giorgini

Dipartimento di Fisica, Università di Trento and CNR-INO BEC Center, I-38050 Povo, Trento, Italy

(Received 20 June 2012; published 12 November 2012)

The liquid and crystal phases of a single-component Fermi gas with dipolar interactions are investigated using quantum Monte Carlo methods in two spatial dimensions and at zero temperature. The dipoles are oriented by an external field perpendicular to the plane of motion, resulting in a purely repulsive $1/r^3$ interaction. In the liquid phase we calculate the equation of state as a function of the interaction strength and other relevant properties characterizing the Fermi-liquid behavior: effective mass, discontinuity at the Fermi surface, and pair correlation function. In the high density regime we calculate the equation of state of the Wigner crystal phase and the critical density of the liquid to solid quantum phase transition. Close to the freezing density we also search for the existence of a stripe phase, but such a phase is never found to be energetically favorable.

DOI: 10.1103/PhysRevLett.109.200401 PACS numbers: 05.30.Fk, 03.75.Hh, 03.75.Ss

The recent rapid developments in the field of ultracold dipolar atoms and molecules have opened up new fascinating prospects for investigating many-body effects in quantum degenerate gases with long-range interactions (for a review see, e.g., Ref. [1]). In this respect, single-layer and multilayer configurations of two-dimensional fermions are particularly intriguing because of the competing interplay, depending on the strength of the dipolar interaction and on the distance between layers, between Fermi-liquid behavior, superfluid pairing, crystal order, and density-wave instabilities [2–11].

Fermionic molecules of $^{40}K^{87}Rb$, which can have a strong electric dipole moment, have been created using coherent transfer of Feshbach molecules to their rovibrational ground state [12] and have been brought toward the quantum degenerate regime [13]. Other fermionic molecules are now being actively studied experimentally [14,15]. Atomic species with a large magnetic moment, such as dysprosium, offer a different possibility of realizing degenerate Fermi gases of dipoles which was successfully pursued, although for the moment only in the weakly interacting regime, in the experiment of Ref. [16].

A particularly simple geometrical arrangement of a single-component dipolar Fermi gas in 2D is when the dipoles are oriented perpendicular to the plane of motion by means of a sufficiently strong external field. This configuration has been proven to greatly suppress the chemical reaction rate of molecules, thereby enhancing their lifetime [17]. Here particles at distance r interact via a purely repulsive, rotationally symmetric, and long range $1/r^3$ potential. Still the phase diagram at zero temperature is expected to be quite rich: interlayer dimers and a novel BCS-BEC superfluid crossover are predicted in bilayer systems [5], while in-plane and out-of-plane density ordered phases are predicted in multilayer systems [6,7]. In the case of a single layer, a Fermi liquid with peculiar scattering properties is stable at low density [10] and a Wigner crystal emerges at high density, where the classical potential energy of dipoles largely exceeds their kinetic energy. For intermediate values of the interaction strength an instability at finite wave vector is predicted to set in [3,4,9], driving the system to a stripe phase that breaks both rotational and translational symmetry (in the direction perpendicular to the stripes). A similar scenario, involving microemulsion phases (e.g., stripes or bubbles), is expected for the melting of the Wigner crystal at $T = 0$ in a 2D Coulomb gas [18]. These results are derived within a mean-field approach: an important question concerns the quantitative determination of the phase diagram using more accurate theoretical tools, such as quantum Monte Carlo (QMC) techniques [19].

In this Letter we examine a 2D system of N identical fermionic particles of mass m that interact with the Hamiltonian

$$H = -\frac{\hbar^2}{2m}\sum_i \nabla_i^2 + \sum_{i<j}\frac{d^2}{r_{ij}^3}, \tag{1}$$

where r_{ij} is the distance between particle i and j, and d is the intensity of the electric (or magnetic) dipole moment. The strength of the dipolar interaction is conveniently expressed in terms of the dimensionless parameter $k_F r_0$, where $r_0 = md^2/\hbar^2$ is the characteristic length of the dipole-dipole force and $k_F = \sqrt{4\pi n}$ is the Fermi wave vector of the 2D gas determined by the density n. The energy scale set by k_F is the Fermi energy $\epsilon_F = \hbar^2 k_F^2/2m$. As a function of $k_F r_0$ we investigate the ground-state properties of the Fermi-liquid phase including the equation of state, the effective mass, the discontinuity of the momentum distribution at k_F, the pair correlation function, and the static structure factor. By comparing the energy of the Fermi liquid (FL) and of the Wigner crystal (WC) phase, we determine the value $k_F r_0 = 25 \pm 3$ of the freezing density. Furthermore, in the region of interaction

strengths close to freezing, we calculate the energy corresponding to a stripe phase finding that it is never favorable compared to the FL and WC state. The main results on the equation of state are shown in Fig. 1 in units of the Hartree-Fock energy

$$E_{\mathrm{HF}} = N\frac{\epsilon_F}{2}\left(1 + \frac{128}{45\pi}k_F r_0\right), \tag{2}$$

corresponding to the lowest order perturbation expansion of the FL in the interaction parameter $k_F r_0$ [3,10].

We use the fixed-node diffusion Monte Carlo (FN-DMC) method, a projector technique that, starting from an antisymmetric trial wave function ψ_T, finds the state having the lowest energy compatible with the many-body nodal surface of ψ_T that is kept fixed during the calculation. The method provides a rigorous upper bound to the energy of the fermionic ground state [20].

Simulations are performed in a box of volume $V = L_x L_y$, where we always take $L_x \leq L_y$. The density is $n = N/V$ and we use periodic boundary conditions (PBCs) in both spatial directions. Since the dipole-dipole interaction is long range, the potential energy contribution to the Hamiltonian, given by the second term in Eq. (1), requires a careful treatment

$$V_{dd} = \sum_{i<j}\frac{d^2}{|\mathbf{r}_i - \mathbf{r}_j|^3} + \frac{1}{2}\sum_{i,j}\sum_{\mathbf{R}\neq 0}\frac{d^2}{|\mathbf{r}_i - \mathbf{r}_j - \mathbf{R}|^3}, \tag{3}$$

where i and j label particles in the simulation cell and the vectors $\mathbf{r}_{i(j)} + \mathbf{R}$ correspond to the positions of all images

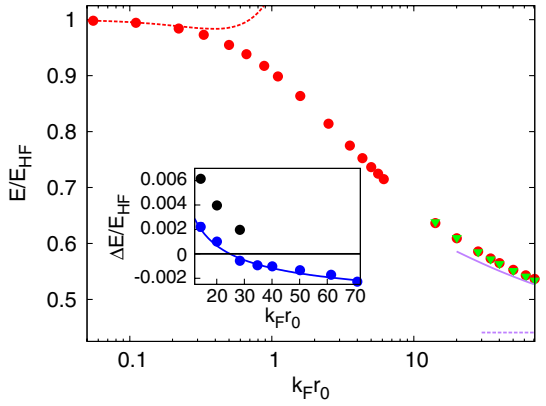

FIG. 1 (color online). Equation of state of the liquid and solid phase in units of the Hartree-Fock energy (2). Red circles refer to the liquid and green triangles to the solid. The red dashed line corresponds to the second-order expansion in Ref. [10]. The purple dashed horizontal line and solid line correspond, respectively, to the classical energy of the Wigner crystal and to the result of Ref. [29] including the first correction arising from the zero-point motion of phonons. Inset: Energy difference between the solid and the liquid (blue circles) and between the stripe phase and the liquid (black circles). The blue solid line is obtained from a best fit to the equation of state of the liquid and solid phase. Error bars are smaller than the size of the symbols and are comparable in the three phases.

of particle $i(j)$ in the array of replicas of the simulation cell. The combination of all images has the same average density n of the simulation box and provides a good approximation of the homogeneous medium. In the case of the Coulomb potential the summation in (3) is carried out by means of the Ewald method [20]. For the faster convergent $1/r^3$ potential, the mean interaction energy can be evaluated using the simpler formula

$$\langle V\rangle = (V_{dd})_{R_c} + V_{\mathrm{tail}}, \tag{4}$$

where $(V_{dd})_{R_c}$ denotes the sum (3) with the constraint $|\mathbf{r}_i - \mathbf{r}_j - \mathbf{R}| \leq R_c$ and $V_{\mathrm{tail}} = \pi n d^2/R_c$ is the contribution from distances larger than R_c assuming a uniform distribution of particles. The cut-off length R_c is chosen large enough ($R_c = 2L_x$) to yield an average interaction energy $\langle V\rangle$ that is independent of R_c, within statistical uncertainty.

Fermi-liquid phase.—The trial wave function describing the FL phase is assumed to be of the Jastrow-Slater form

$$\psi_T(\mathbf{r}_1, \ldots, \mathbf{r}_N) = \prod_{i<j} f(r_{ij})\,\det[e^{i\mathbf{k}_\alpha\cdot\mathbf{r}_i}]. \tag{5}$$

Here $\mathbf{k}_\alpha = (2\pi/L)(n_\alpha^x, n_\alpha^y)$ with $n_\alpha^{x,y} = 0, \pm 1, \pm 2, \ldots$ are the wave vectors complying with PBCs in the square box ($L_x = L_y = L$) and $f(r)$ is a non-negative function satisfying the boundary condition $f'(r = L/2) = 0$. The short-range behavior of $f(r)$ is of the form $f(r) \propto K_0(2\sqrt{r_0/r})$, where K_0 is the modified Bessel function, and fulfills the cusp condition of the atomic potential [21].

A delicate issue related to QMC calculations of the equation of state is the extrapolation to the thermodynamic limit (TL). In the FL phase apart from the size dependence affecting the potential energy contribution, which we treat using the procedure in Eq. (4), significative shell effects are present in the kinetic energy contribution. We consider closed-shell configurations corresponding to $25 \leq N \leq 81$ for which the relative error $|\Delta T_N|/E_{\mathrm{TL}}^{(0)} = |E_N^{(0)}/E_{\mathrm{TL}}^{(0)} - 1|$ in the energy of the noninteracting gas compared to the TL can be as large as $\sim 1\%$. An extrapolation method based on FL theory is provided by the fitting formula [22]

$$E_N = E_{\mathrm{TL}} + \frac{m}{m^*}\Delta T_N + \frac{a}{N}, \tag{6}$$

which involves the parameter m/m^*, determining the inverse effective mass of the particles, and the coefficient a of the residual size dependence assumed to be linear in $1/N$. Here E_N is the QMC output energy of the N-particle system with the potential contribution evaluated using Eq. (4). The values of $E_N - \Delta T_N$ are shown as red symbols in Fig. 2. Their scattered dependence on $1/N$ is considerably suppressed if one accounts for the effective mass, as it is shown by the green symbols corresponding to $E_N - (m/m*)\Delta T_N$. A more reliable convergence to the TL is obtained using the method of twist-averaged boundary conditions

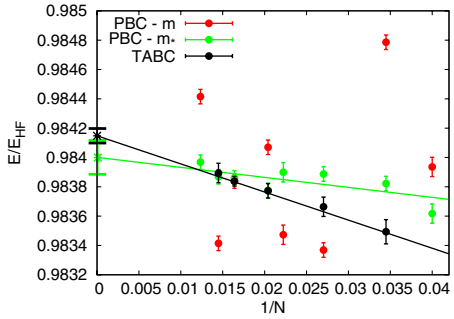

FIG. 2 (color online). Finite size effects in a Fermi liquid at the density $k_F r_0 = 0.22$. The black symbols and line correspond to TABC energies and linear fit. The green symbols and line correspond to PBC energies $E_N - (m/m^*)\Delta T_N$ and linear fit. Red symbols correspond instead to PBC energies $E_N - \Delta T_N$. The values extrapolated to the TL are shown with the corresponding error bars.

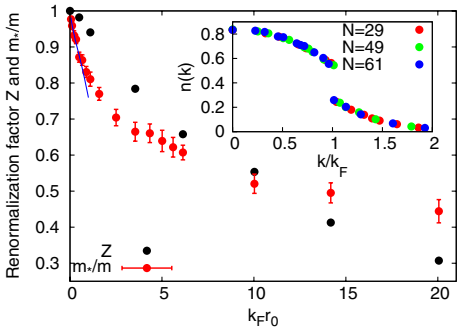

FIG. 3 (color online). Effective mass and renormalization factor in the liquid phase as a function of the interaction strength. The line corresponds to the perturbation expansion for m^*/m of Ref. [10]. Inset: Momentum distribution corresponding to $k_F r_0 = 20$ for different system sizes.

(TABCs) [23]. Here the PBC wave vectors of the plane waves in the Slater determinant of Eq. (5) are replaced by $\mathbf{k}_\alpha(\boldsymbol{\theta}) = (2\pi/L)(n_\alpha^x + \theta_x, n_\alpha^y + \theta_y)$, where θ_x, θ_y are continuous variables in the interval [0, 1]. In the grand canonical implementation of the TABCs described in Refs. [23,24] the wave vectors are constrained by $|\mathbf{k}_\alpha(\boldsymbol{\theta})| < k_F$ and different values of the twist $\boldsymbol{\theta}$ can correspond to different numbers of particles. The number of particles $\bar{N}$ and the energy $E_{\bar{N}}$ are obtained from averages over all possible twist angles. With our use of TABCs we still find a residual size effect $\Delta T_{\bar{N}}$ [25]. The extrapolation to the TL is performed using Eq. (6) and statistical agreement in E_{TL} between PBCs and TABCs is obtained for all values of the density (see Fig. 2).

The FN-DMC results of the ground-state energy using TABCs are reported in Fig. 1. At low density we find good agreement with the result $E = E_{\mathrm{HF}} + (N\epsilon_F/8)(k_F r_0)^2 \times \log(1.43 k_F r_0)$, which was derived in Ref. [10] including corrections to the lowest order expansion (2).

The effective mass m^* obtained from Eq. (6) is shown in Fig. 3 for different values of $k_F r_0$. At weak coupling our results well reproduce the perturbation expansion reported in Ref. [10], but for larger couplings the reduction of m^* is less pronounced than the perturbative prediction and m^*/m approaches the value 0.4 for $k_F r_0$ close to freezing. From the discontinuity at k_F of the momentum distribution parametrized by $n_k = Z\theta(k_F - k) + g(k)$, where $\theta(x)$ is the step function and $g(k)$ is a continuous function of k, we extract the renormalization factor Z. Results are reported in Fig. 3. In the inset of Fig. 3 we show n_k in the strongly interacting regime for different numbers of particles. It is worth noticing that finite size effects on this quantity are much less severe here than in the 2D Coulomb gas [26] and are similar to the case of the hard disks investigated in Ref. [27].

Finally, we calculate the pair correlation function $g(r)$ giving the probability of finding two particles at the distance r. Results for different values of $k_F r_0$ in the FL phase are shown in Fig. 4. One should notice that by increasing the interaction strength the short-range repulsion increases and a shell structure starts to appear on approaching the freezing density. The Fourier transform of $g(r)$ yields the static structure factor $S(\mathbf{k}) = 1 + n \int d\mathbf{r} e^{i\mathbf{k}\cdot\mathbf{r}}[g(r) - 1]$. This quantity can also be calculated directly in the FN-DMC algorithm by evaluating the average of the product of density fluctuation operators $NS(\mathbf{k}) = \langle \rho_{\mathbf{k}} \rho_{-\mathbf{k}} \rangle = \langle \sum_{i,j} e^{i\mathbf{k}\cdot(\mathbf{r}_i - \mathbf{r}_j)} \rangle$. Results are reported in Fig. 5 for both estimators [28]. For large values of $k_F r_0$, the direct estimator exhibits a more pronounced peak compared to the smoother Fourier transform at the wave vector corresponding to the lowest nonzero reciprocal lattice vector of the triangular lattice.

Wigner crystal phase.—To describe the WC phase we make use of the following trial wave function

$$\psi_T(\mathbf{r}_1, \ldots, \mathbf{r}_N) = \prod_{i<j} f(r_{ij}) \det[e^{-(\mathbf{r}_i - \mathbf{R}_m)^2/\alpha^2}], \qquad (7)$$

where the Jastrow correlation term $f(r)$ is the same as in the FL phase and the single-particle orbitals in the determinant are constructed with Gaussians, whose width α is a

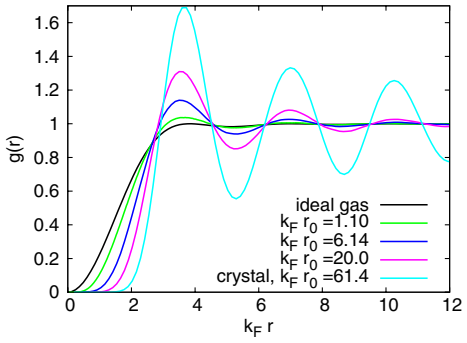

FIG. 4 (color online). Pair correlation function in the liquid and in the crystal phase. The pair correlation function of the noninteracting gas is also shown.

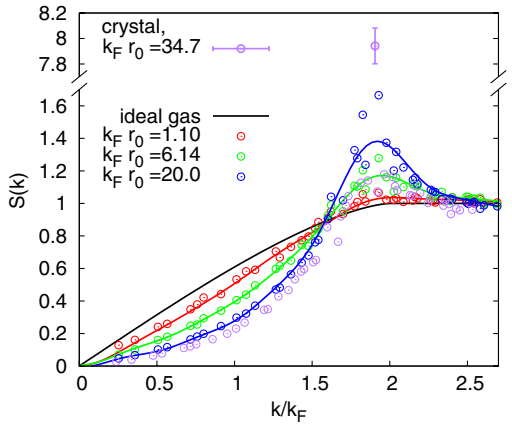

FIG. 5 (color online). Static structure factor in the liquid and in the crystal phase ($N = 56$). In the liquid phase, solid lines correspond to the Fourier transform of $g(r)$ while symbols correspond to the direct calculation of $S(k)$. The static structure factor of the noninteracting gas is also shown.

variational parameter, centered at the lattice points $\mathbf{R}_m$ of the triangular Bravais lattice. In order to enforce PBCs, both the number of particles N and the box sizes L_x and L_y must be multiples of a primitive cell, which can be chosen as a rectangle of side lengths $\ell_y = \sqrt{3}\ell_x$ containing two atoms. Extrapolation to the thermodynamic limit is obtained using a linear fit in $1/N$ over the FN-DMC energies. The results for the WC equation of state are reported in Fig. 1. It is worth noticing that the antisymmetric constraint imposed in the wave function (7) for particle exchange is negligible for the value of the energy. In fact, statistically compatible results are obtained with a nodeless wave function of distinguishable boltzmanons in agreement with the findings of Ref. [21]. This behavior is expected at large density, where the energy of the WC phase is given by the result [29]

$$E_{\mathrm{WC}} = N\frac{\epsilon_F}{2}\frac{k_F r_0}{4}\left(1.597 + \frac{2.871}{\sqrt{k_F r_0}}\right), \tag{8}$$

obtained by including the contribution from the zero-point motion of phonons to the purely classical interaction energy of a system of dipoles arranged in a triangular Bravais lattice. The above expansion, holding for large $k_F r_0$, is shown in Fig. 1 and is indeed approached by our QMC results. The difference between the ground-state energy of the WC and FL phase is shown in the inset of Fig. 1. From a fit to the equation of state of the two phases we can determine the intersection point at $k_F r_0 = 25 \pm 3$. This value is almost a factor two smaller compared to the critical density $k_F r_0 \sim 60$ [21,29,30] of an equivalent system of bosons having the same mass, density, and dipolar strength. This can be understood if one considers that the equation of state of the crystal is practically independent of statistics while the energy of the fermionic fluid is significantly higher than the bosonic one. Large values of $k_F r_0$ should be achievable in future experiments with polar molecules having large electric dipole moments, such as NaK [14]. From the equation of state of the FL and WC phase in the vicinity of the freezing density one can also estimate the width of the region where phase separation occurs. By imposing equilibrium of pressure and chemical potential in the two phases, the coexistence region turns out to be $\delta(k_F r_0) \sim 0.01$, a very small value consistent with a similar finding in the bosonic case [29]. We notice that, according to Ref. [18], the value of $\delta(k_F r_0)$ sets the range of densities where microemulsion phases, which drive the liquid to solid transition, are predicted to appear. The pair correlation function and the static structure factor deep in the crystal phase are shown respectively in Fig. 4 and 5. In particular, $S(\mathbf{k})$ exhibits a large peak at $k = 1.90 k_F$ corresponding to the lowest nonzero wave vector of the reciprocal lattice.

Stripe phase.—A pattern of equally spaced stripes is assumed in the y direction corresponding to the trial wave function

$$\psi_T(\mathbf{r}_1, \ldots, \mathbf{r}_N) = \prod_{i<j} f(r_{ij}) \det[e^{ik_{\alpha x} x_i - (y_i - y_a)^2/\gamma^2}], \tag{9}$$

where the Jastrow factor is the same as in the FL and WC phase, y_a denotes the y coordinate of the ath stripe and $k_{\alpha x} = 2\pi n_{\alpha x}/L_x$ are the PBC wave vectors in the x direction. The number of fermions is the same in each stripe and once multiplied by the number of stripes determines the overall density in the volume $V = L_x L_y$. First, using the variational method, we optimize the width γ of the stripes and their separation $\Delta y = |y_{a+1} - y_a|$. For the latter quantity we find that $k_F \Delta y = \sqrt{4\pi}$ is an optimal value corresponding to a square box having $L_x = L_y$. We then perform FN-DMC simulations using PBCs with different numbers of particles N and we extrapolate to the thermodynamic limit relying on a $1/N$ linear fit. The results are shown in the inset of Fig. 1, where we report the energy difference between the stripe and FL phase. For all values of $k_F r_0$ in the vicinity of the freezing density the stripe phase is never energetically favorable compared to the FL or the WC phase.

In conclusion, we investigated the ground state of a purely repulsive system of dipolar fermions and its liquid to solid transition. Important extensions of this work concern the effect of a tilting angle, making the interaction in the 2D plane anisotropic, and the coupling to a second layer inducing interlayer attraction.

Useful discussions with G. Astrakharchik, M. Holzmann, and M. Capone are gratefully acknowledged. This work has been supported by ERC through the QGBE grant. Calculations were performed on the AURORA supercomputer at Fondazione Bruno Kessler.

[1] M. A. Baranov, Phys. Rep. **464**, 71 (2008).
[2] G. M. Bruun and E. Taylor, Phys. Rev. Lett. **101**, 245301 (2008).
[3] Y. Yamaguchi, T. Sogo, T. Ito, and T. Miyakawa, Phys. Rev. A **82**, 013643 (2010).
[4] K. Sun, C. Wu, and S. Das Sarma, Phys. Rev. B **82**, 075105 (2010).
[5] A. Pikovski, M. Klawunn, G. V. Shlyapnikov, and L. Santos, Phys. Rev. Lett. **105**, 215302 (2010).
[6] N. T. Zinner and G. M. Bruun, Eur. Phys. J. D **65**, 133 (2011).
[7] M. Babadi and E. Demler, Phys. Rev. B **84**, 235124 (2011).
[8] L. M. Sieberer and M. A. Baranov, Phys. Rev. A **84**, 063633 (2011).
[9] M. M. Parish and F. M. Marchetti, Phys. Rev. Lett. **108**, 145304 (2012).
[10] Z.-K. Lu and G. V. Shlyapnikov, Phys. Rev. A **85**, 023614 (2012).
[11] J. K. Block, N. T. Zinner, and G. M. Bruun, New J. Phys. **14**, 105006 (2012).
[12] K.-K. Ni, S. Ospelkaus, M. H. G. de Miranda, A. Pe'er, B. Neyenhuis, J. J. Zirbel, S. Kotochigova, P. S. Julienne, D. S. Jin, and J. Ye, Science **322**, 231 (2008).
[13] S. Ospelkaus, K.-K. Ni, D. Wang, M. H. G. de Miranda, B. Neyenhuis, G. Qumner, P. S. Julienne, J. L. Bohn, D. S. Jin, and J. Ye, Science **327**, 853 (2010).
[14] J. W. Park, C.-H. Wu, I. Santiago, T. G. Tiecke, S. Will, P. Ahmadi, and M. W. Zwierlein, Phys. Rev. A **85**, 051602 (R) (2012).
[15] M.-S. Heo, T. T. Wang, C. A. Christensen, T. M. Rvachov, D. A. Cotta, J.-H. Choi, Y.-R. Lee, and W. Ketterle, Phys. Rev. A **86**, 021602(R) (2012).
[16] M. Lu, N. Q. Burdick, and B. L. Lev, Phys. Rev. Lett. **108**, 215301 (2012).
[17] K.-K. Ni, S. Ospelkaus, D. Wang, G. Quemener, B. Neyenhuis, M. H. G. de Miranda, J. L. Bohn, J. Ye, and D. S. Jin, Nature (London) **464**, 1324 (2010).
[18] B. Spivak and S. A. Kivelson, Phys. Rev. B **70**, 155114 (2004).
[19] For the 2D Coulomb gas see B. K. Clark, M. Casula, and D. M. Ceperley, Phys. Rev. Lett. **103**, 055701 (2009).
[20] For more details see, e.g., J. Kolorenč and L. Mitas, Rep. Prog. Phys. **74**, 026502 (2011).
[21] G. E. Astrakharchik, J. Boronat, I. L. Kurbakov, and Yu. E. Lozovik, Phys. Rev. Lett. **98**, 060405 (2007).
[22] D. M. Ceperley, Phys. Rev. B **18**, 3126 (1978).
[23] C. Lin, F. H. Zong, and D. M. Ceperley, Phys. Rev. E **64**, 016702 (2001).
[24] S. Chiesa, D. M. Ceperley, R. M. Martin, and M. Holzmann, Phys. Rev. Lett. **97**, 076404 (2006).
[25] The residual kinetic energy size error $\Delta T_{\bar{N}}$ is too small to allow for a meaningful extraction of the effective mass ratio m^*/m.
[26] M. Holzmann, B. Bernu, V. Olevano, R. M. Martin, and D. M. Ceperley, Phys. Rev. B **79**, 041308(R) (2009).
[27] N. D. Drummond, N. R. Cooper, R. J. Needs, and G. V. Shlyapnikov, Phys. Rev. B **83**, 195429 (2011).
[28] The functions n_k, $g(r)$ and $S(k)$ have been calculated using the extrapolation customary in DMC techniques [20].
[29] C. Mora, O. Parcollet, and X. Waintal, Phys. Rev. B **76**, 064511 (2007).
[30] H. P. Büchler, E. Demler, M. Lukin, A. Micheli, N. Prokof'ev, G. Pupillo, and P. Zoller, Phys. Rev. Lett. **98**, 060404 (2007).